OPTICA

On-demand terahertz surface wave generation with microelectromechanical-system-based metasurface

Chunxu Chen,[1,†] Kelson Kaj,[2,†] Xiaoguang Zhao,[1,3,†] Yuwei Huang,[4] Richard D. Averitt,[2,5] and Xin Zhang[1,4,*]

[1]Department of Mechanical Engineering, Boston University, Boston, Massachusetts 02215, USA
[2]Department of Physics, University of California, San Diego, La Jolla, California 92093, USA
[3]Currently with Department of Precision Instruments, Tsinghua University, Beijing 100084, China
[4]Division of Materials Science and Engineering, Boston University, Boston, Massachusetts 02215, USA
[5]e-mail: raveritt@ucsd.edu
*Corresponding author: xinz@bu.edu

Received 6 October 2021; revised 23 November 2021; accepted 23 November 2021; published 22 December 2021

During the past decade, metasurfaces have shown great potential to complement standard optics, providing novel pathways to control the phase, amplitude, and polarization of electromagnetic waves utilizing arrays of subwavelength resonators. We present dynamic surface wave (SW) switching at terahertz frequencies utilizing a mechanically reconfigurable metasurface. Our metasurface is based on a microelectromechanical system (MEMS) consisting of an array of micro-cantilever structures, enabling dynamic tuning between a plane wave (PW) and a SW for normal incidence terahertz radiation. This is realized using line-by-line voltage control of the cantilever displacements to achieve full-span (2π) phase control. Full-wave electromagnetic simulations and terahertz time-domain spectroscopy agree with coupled mode theory, which was employed to design the metasurface device. A conversion efficiency of nearly 60% has been achieved upon switching between the PW and SW configurations. Moreover, a nearly 100 GHz working bandwidth is demonstrated. The MEMS-based control modality we demonstrate can be used for numerous applications, including but not limited to terahertz multifunctional metasurface devices for spatial light modulation, dynamic beam steering, focusing, and beam combining, which are crucial for future "beyond 5G" communication systems.

https://doi.org/10.1364/OPTICA.444999

1. INTRODUCTION

The arbitrary control of electromagnetic (EM) waves is one of the key aims in modern photonics and antenna research [1,2]. Moreover, the "on-demand" control of EM waves is a challenging and important task to realize next-generation communication systems [3–6]. Conventional optical components, such as lenses, wave plates, optical modulators, and mirrors typically rely on wave propagation over distances that are much greater than the wavelength to shape wavefronts or change the wave amplitude, phase, and polarization [7]. In contrast, metamaterials (MMs) are subwavelength EM composites that have enabled new pathways to control the propagation of EM waves [8–12]. Compared with standard optical components, MM devices can be compact and lightweight, an important goal for the increasingly demanding requirements in miniaturization of modern EM and photonic systems. MMs are typically created by designing an array of subwavelength unit cells forming a composite with an effective permittivity and permeability to achieve novel properties that have enabled various applications and groundbreaking phenomena that cannot be realized in natural materials [13–19].

In addition, metasurfaces (the two-dimensional analog of MMs) have attracted considerable attention due to the relative ease of fabrication and versatility in manipulating EM waves [20–25]. Notably, among different metasurface devices, an important development is the implementation of phase-gradient unit cells to realize functional Huygens's surfaces in an ultrathin structure ($\sim 1/100\lambda$) [26–33]. However, the majority of phase-gradient metasurfaces realized to date are static, responding to incident waves in a prescribed manner and lacking real-time tunability. Adding real-time on-demand functionality to metasurfaces would enable dynamic control of EM waves and novel routes to reconfigure optical components. Previous research has demonstrated tunability in metasurfaces using various approaches. This includes phase change materials (PCMs, like $Ge_2Sb_2Te_5$ and VO_2) [34–36], optically tunable semiconductors [37], electrical gating [38], 2D materials [39], among others. These tuning approaches enable high-efficiency manipulation of the metasurface response by controlling the constituent material properties to tailor the propagation characteristics of EM waves at comparatively high speeds. As a complementary approach, MEMS may also be employed to modify the structure of the metasurface unit cells, providing novel degrees of freedom to tune the metasurface response. For example, by integrating basic MEMS components such as voltage tunable micro-cantilevers [40–42], bi-material cantilevers [43],

and comb-drive structures [44,45] with metasurfaces [46–48], different tunable devices can be achieved. Importantly, recent research has also demonstrated the considerable potential of MEMS-tunable metasurface devices for wavefront engineering and polarization control [49,50], giving rise to flat lenses for sub-wavelength focusing [51,52], polarization conversion [53], and arbitrary vector-beam generation [54].

We present the design, fabrication, and characterization of a MEMS-based metasurface with a controllable phase gradient that can dynamically switch between plane wave (PW) and surface wave (SW) states in the terahertz frequency band (measured using terahertz time-domain spectroscopy, THz-TDS). Our theoretical analysis based on coupled mode theory (CMT) [55], the generalized law of reflection, and finite element simulations provide a comprehensive view of the tunable EM response. Compared with previous research using MEMS cantilever-based metasurfaces [56–58], our work demonstrates that the line-by-line control (1D control) can be realized. Importantly, the MEMS-based metasurface proposed here can effectively convert the PW to SW with nearly 60% conversion efficiency over a ~ 100 GHz working bandwidth. This work demonstrates that on-demand switching capabilities can be realized with MEMS-based micro-cantilever structures to manipulate the phase, amplitude, and directionality of EM waves. The theoretical analysis, fabrication, finite element simulation results, and THz-TDS measurement results of our MEMS-based metasurface are presented in the following sections.

2. COUPLED MODE THEORY DESCRIPTION OF MEMS-BASED METASURFACE

The working principle of the MEMS-based metasurface is shown in Fig. 1(a). The metasurface consists of a three-layer metal-insulator-metal (MIM) structure. The top layer is a suspended cantilever structure, which serves as the reconfigurable metallic resonator, where the tip height (d) can be changed by applying an electrostatic force with an external actuation voltage. The silicon substrate serves as the dielectric spacer, while the continuous gold plane acts as a ground plane. Due to the existence of the gold ground plane, the transmission is negligible, and we only need to consider the reflection (R) in the following analysis. CMT is used to analyze the response of the MEMS-based metasurface. CMT is typically used to study the coupling of a resonator to one or more ports, or to other resonators. However, in our metasurface device, the resonances are spectrally separated, and the only resonance of concern is that of the reconfigurable cantilever metasurface (RCMS). As a result, a one-port single-mode model in CMT can fully describe the EM response of the RCMS. The reflection coefficient can be expressed by the following equation [42]:

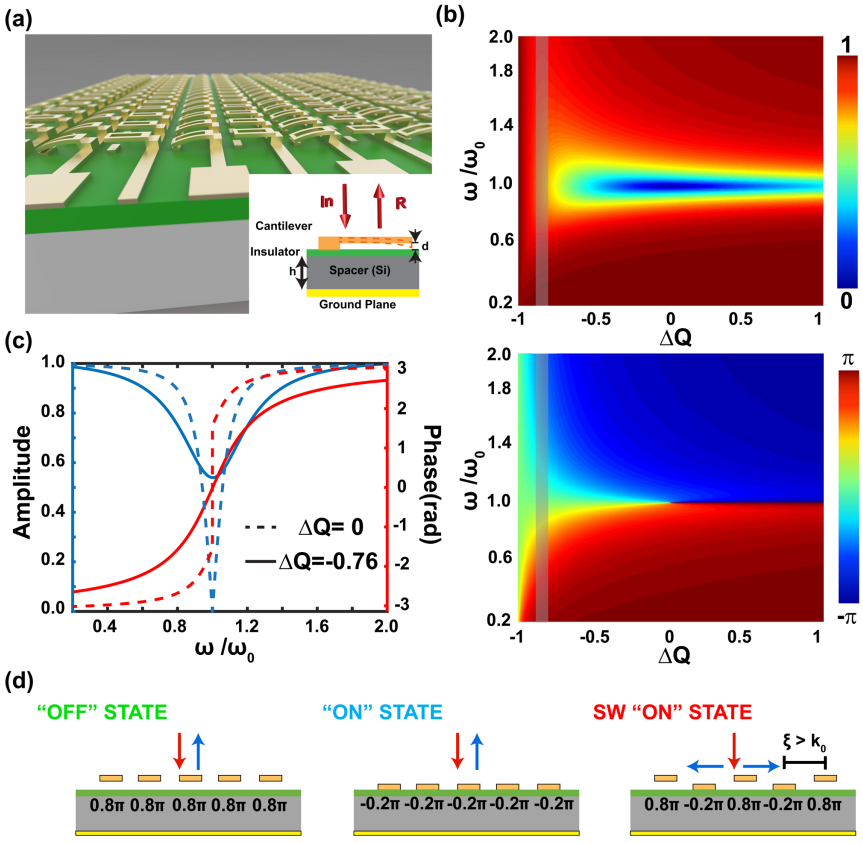

Fig. 1. Reconfigurable cantilever metasurface (RCMS) structure and working principle. (a) Schematic drawing of the RCMS in the SW "ON" state. Inset: cross-sectional RCMS unit cell in the one-port system showing the incident (In) radiation and the corresponding reflection (R). (b) Reflection amplitude (top) and phase (bottom) of RCMS for different resonance frequencies (ω/ω_0) and quality factors ($\Delta Q = (Q_r - Q_a)/Q_a$) calculated using CMT. (c) The amplitude (blue) and phase response (red) versus resonance frequencies for $\Delta Q = -0.76$ (solid lines) [corresponding to the vertical shaded band in (b)] and $\Delta Q = 0$ (dashed lines). (d) Schematic of RCMS operation. The left image depicts the "OFF" state with no voltage actuation; the middle image depicts all cantilevers actuated (see data and simulations in Fig. 3 and 4); and the right image is with every other row of cantilevers actuated, enabling plane wave to surface wave conversion (see Fig. 5 for details).

$$r = -1 + \frac{1/Q_r}{-i(\omega-\omega_0)/\omega_0 + 1/(2Q_a) + 1/(2Q_r)}, \quad (1)$$

where ω_0 is the resonance frequency and Q_a and Q_r are the absorptive and radiative quality factors, respectively. The resonance frequency (ω_0) is determined by the mode supported by the metasurface unit cell. The absorptive quality factor (Q_a) is defined as the ratio of total stored energy in a metasurface unit cell to the time-averaged energy, while the radiative quality factor (Q_r) is the ratio of the total energy and the energy radiated by the unit cell per oscillation cycle. The radiative and the absorptive quality factors can be numerically determined by Eqs. (2) and (3), respectively [59]:

$$Q_r = \frac{1}{2k_0 h}\sum \Gamma(m)\frac{\sin^2(m\pi a/p)}{(m\pi a/p)^2}, \quad (2)$$

$$Q_a = \frac{\mathrm{Re}(\varepsilon)hp}{\alpha \mathrm{Im}(\varepsilon)hp + \beta(2p-a)H(\delta)}, \quad (3)$$

where k_0 is the free space wavenumber, h is the spacer thickness, p is the unit cell periodicity, and a is the slit width on the top layer of the metasurface. As can be seen from Eqs. (2) and (3), in addition to the geometrical and material parameters of the resonator, the spacer thickness h plays a dominant role in determining the radiative and absorptive quality factors, where the radiative quality factor Q_r scales inversely to h and the absorptive quality factor Q_a depends quasilinearly on h. In our RCMS, by changing the tip height (d), the effective spacer thickness $h+d$ can be changed, which, in turn, modifies the radiative quality factor Q_r, absorptive quality factor Q_a, and reflection coefficient.

For the sake of generality, we define two dimensionless factors ω/ω_0 and $\Delta Q = (Q_r - Q_a)/Q_a$ to describe the response of the MEMS-based metasurface at an arbitrary frequency (ω). As shown in Fig. 1(b), the reflection amplitude and phase for different ω/ω_0 and ΔQ demonstrate that the phase and amplitude response can be fully controlled by tuning the frequency (ω) for a given ΔQ value. Importantly, in order to generate a SW (and, more generally, realize other beam-forming control strategies with RCMSs), it is desirable to have smooth control of the phase change over a full-span of 2π while simultaneously achieving minimal changes in the reflection amplitude in the RCMS. For example, when $\Delta Q = 0$, the phase can be changed from $-\pi$ to π by sweeping the frequency (ω). However, the reflection amplitude varies from 1 to 0 (perfect absorption) for $\Delta Q = 0$, which is unwanted for SW generation. When $\Delta Q > 0$ (see Supplement 1), where the resonance of the unit cell is overdamped by the strong absorption, the phase shows a sudden jump from positive to negative for an increasing ω, thereby lacking a smooth phase change. However, when $\Delta Q < 0$, an underdamped condition is achieved. For underdamping, a gradual phase change from $-\pi$ to π can be achieved by changing the frequency (ω) [see the lower plot of Fig. 1(b)] which, as stated above, is important in designing a RCMS to generate a SW. It is noteworthy that the variation in amplitude is also minimized for increasingly negative ΔQ values. However, if ΔQ is too negative, the phase change as a function of ω/ω_0 may be too slow, requiring a large frequency tuning range beyond the modulation range of our current RCMS. As a result, a balance point for the selection of ΔQ is required to optimize the phase and amplitude response. Figure 1(c) shows the tuning range of the amplitude and phase for a trade-off value of $\Delta Q = -0.76$ (solid line). Comparing with $\Delta Q = 0$ (dashed line), the amplitude modulation is dramatically decreased, and the phase variation becomes much smoother with $\Delta Q = -0.76$. As a result, in order to fulfill the requirements of the underdamped condition ($Q_r < Q_a$, $\Delta Q < 0$) and realize the RCMS to generate SW, it is extremely important to choose the right initial spacer thickness h. However, owing to the trade-off in mechanical strength, fabrication limitations, and the optimal ΔQ value, the silicon spacer thickness is chosen to be 20 μm to achieve the full-span (2π) phase coverage, large resonance frequency shift, and small variation in the reflection amplitude. (see Supplement 1 for a detailed study on choosing the right spacer thickness).

3. SURFACE WAVE GENERATION

In order to generate a SW from a normal incidence PW using the RCMS, two requirements need to be fulfilled. First, the metasurface should remain in the underdamped condition ($\Delta Q < 0$) when the cantilevers deform. The underdamped condition ensures a gradual phase change and the ability to cover the entire 2π range with a relatively small change in the reflection amplitude. In our RCMS structure, ΔQ ranges from -0.17 at the pull-in state to -0.48 at the initial state, while staying in the underdamped region without any phase discontinuity (see Supplement 1 for detailed ΔQ values as a function of cantilever deformation).

The second condition requires a super cell periodicity (P) that is smaller than the targeted free space wavelength (λ_0). A super cell is defined as the composite unit cell that spans a phase of 2π. The second requirement is based on the intrinsic properties of the SW and generalized laws of reflection. The lateral control of the surface phase profile allows for momentum matching to enable the generation of a surface wave that propagates parallel to the surface. The SW is a special type of EM wave that is bounded at an interface and coupled with charge oscillations [60]. Consequently, the radiation pattern of the metasurface can be obtained by solving the Maxwell equations to obtain the following result:

$$E(r,t) = (\mu_0 J_0 c/2k_0)\cdot\left(-\sqrt{k_0^2-\xi^2}\hat{x} + \xi\hat{z}\right) \times e^{i\xi x}e^{i\sqrt{k_0^2-\xi^2}z}e^{-i\omega t}, \quad (4)$$

where $k_0 = 2\pi/\lambda_0$ is the free space wave vector possessed by the normal incidence PW, and $\xi = 2\pi/P$ is the parallel wave vector induced from the RCMS. From Eq. (4), when $\xi < k_0$, the attenuation term ($e^{i\sqrt{k_0^2-\xi^2}z}$) is a complex number, indicating the radiated wave is a PW. However, when $\xi > k_0$, the attenuation term is a real number, showing that the radiated wave becomes a SW. The same results can also be realized with the generalized law of reflection. Based on the Snell's law and Fermat's principle, the reflection angle for a normal incidence beam is determined by $\theta_r = \arcsin(\xi/k_0)$. As a result, the SW is generated when $\xi > k_0$, where the reflection angle is larger than 90°.

By implementing line-by-line voltage control of the tip-pad displacement (d) of the RCMS, the phase difference between the adjacent cantilever-based unit cells is approximately π. As shown in Fig. 1(d), when the metasurface is in the "OFF" state (left), all of the cantilevers are at the initial state. When the voltage is applied to all lines simultaneously, the metasurface is in the "ON" state (middle) with all of the cantilevers pulled to the surface. For this "OFF" and "ON" state, the incident PW will reflect to free space (and the detector). However, when the metasurface is in the SW

"ON" state [right and Fig. 1(a)], the external voltage is applied to every other line of cantilevers, while no voltage is applied to the other lines of cantilevers (i.e., every other row of cantilevers is displaced). By doing so, a nearly π phase difference between adjacent lines is achieved.

4. MATERIALS AND METHODS

The RCMS device was fabricated using surface and bulk micromachining as shown in Figs. 2(a)–2(f). The slightly doped silicon-on-insulator (SOI) wafer was first coated with 400 nm of silicon nitride (SiNx) on both sides. The SiNx layers serve as an insulator and mask layer for the following processes [Fig. 2(a)]. Next, photolithography was performed on the top side of the wafer, followed by reactive ion etching (RIE) to open windows for the ground electrodes [Fig. 2(b)]. The ground electrodes were deposited with 400 nm aluminum through e-beam evaporation and annealing in H_2/N_2 mixing gas to obtain ohmic contact between the metal and silicon. Subsequently, the ground pads and the interconnection wires were patterned with a second round of photolithography, e-beam evaporation, and lift-off using gold [Fig. 2(c)]. Afterwards, an 800 nm thick polyimide film was spin-coated on the surface as a sacrificial layer and then etched through at the anchor position [Fig. 2(d)]. In the next step [Fig. 2(e)], 900 nm copper cantilever structures were patterned on top of the polyimide film using lift-off processing. The rectangular hole on the beam facilitates releasing of the sacrificial layer. Subsequently, the handle layer of the SOI wafer was etched using the potassium hydroxide (KOH) solution resulting in a 20 μm device layer under the metasurface area. The gold ground plane was coated with another e-beam evaporation process to eliminate the transmission. Finally, the sacrificial polyimide layer was completely removed by using O_2 plasma etching [Fig. 2(f)]. Optical microscopy and scanning electron microscopy (SEM) images of the MEMS-based RCMS are shown in Fig. 2(g). The periodicity of the unit cell structure is 120 μm, while for the cantilever beam, the length, width and thickness are 42, 20, and 0.9 μm, respectively. Of note, as shown in Fig. 2(g), due to the residual stress within the beam, the free end of the cantilever tends to bend upwards. Therefore, the initial tip height (d) is ~1.2 μm.

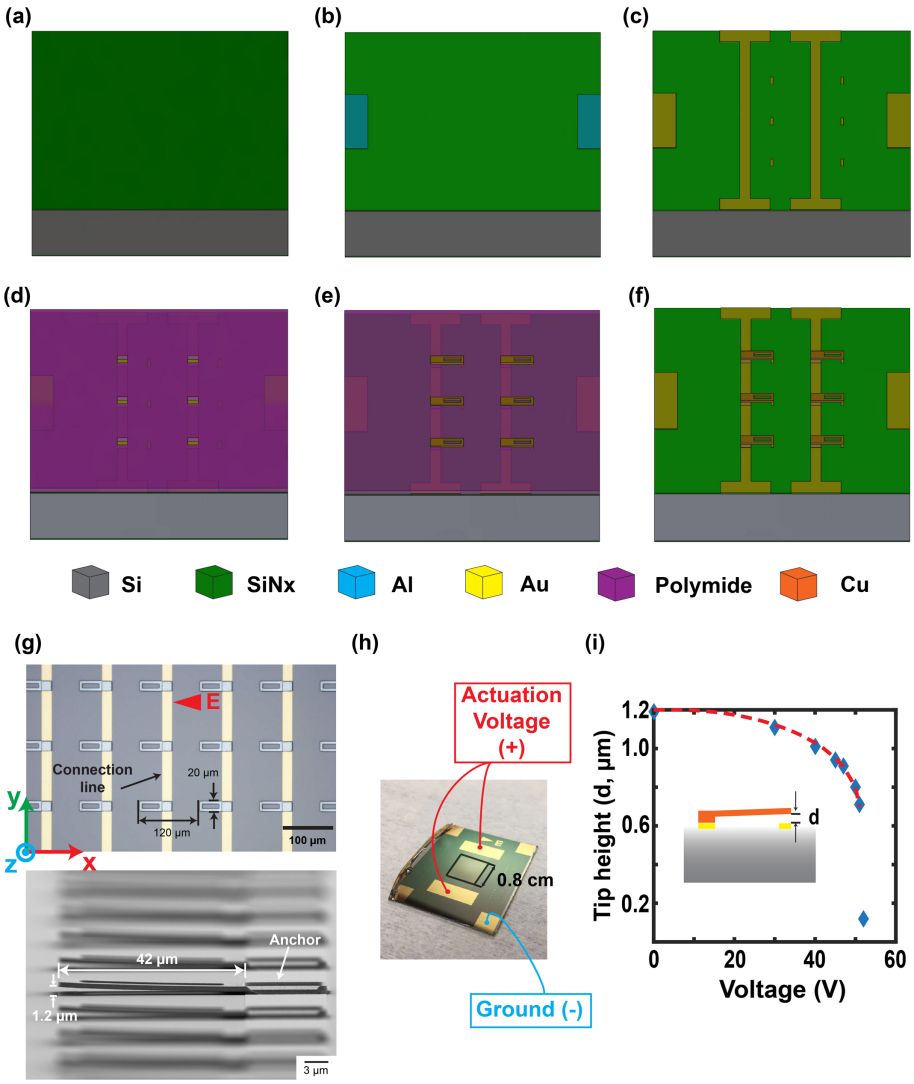

Fig. 2. (a)–(f) Fabrication process flow of the MEMS-based RCMS. (g) Optical microscopy (top) and scanning electron microscope (SEM) image of the MEMS-based RCMS. The E with an arrow shows the e-field polarization direction for the THz-TDS characterization. (h) Photograph of the fabricated device. (i) The measured tip height versus applied DC voltage (blue rhombus). The dashed red line shows the predicted values from simulation (COMSOL 5.3a). The pull-in voltage (V_{PI}) is ~52 V for our design.

As shown in Fig. 2(h), the area of the RCMS is $0.8 \times 0.8\ \text{cm}^2$. After the wafer-scale fabrication, the RCMS is electrically connected to the anode of the source-meter unit (SMU, Keithley 2400 Source-Meter-Unit) through the rectangular gold pads, while the ground electrodes on the corners are connected to the cathode of the SMU. Of note, the top and bottom rectangular pads connect to the different lines on the metasurface, which enables line-by-line control, which is needed for SW control as described above. When an external voltage is applied to the cantilever beams and the silicon substrate, the electrostatic force pulls the suspended cantilevers closer to the substrate. The tip height (d), which is the distance between the bottom side of the cantilever's free end and the top of the gold capacitive pads, is measured with a white-light interferometer (ZYGO NewView 9000). As shown in Fig. 2(i), the tip height decreases with increased DC voltage. However, due to the intrinsic properties of the cantilever structure, the tip height cannot change continuously (see Supplement 1 for mechanical properties of cantilever structure). As a result, beyond a critical voltage (pull-in voltage $V_{\text{PI}} \sim 52$ V), the cantilever snaps down to the capacitive pad, and the RCMS reaches its modulation limit.

The RCMS was measured using THz-TDS in reflection. The THz pulses were generated with a standard photoconductive antenna and a titanium sapphire laser (800 nm, 25 fs pulses, 80 MHz repetition rate). The THz pulses were focused on the metasurface at normal incidence, and the reflected pulses were measured with a second photoconductive antenna. The time-domain response was Fourier transformed to the frequency domain $[E_s(\omega)]$. The reference pulses $[E_r(\omega)]$ were measured with a gold coated silicon substrate. The resolution of the measured reflection data was ~ 6 GHz from 0.5 to 0.75 THz.

The EM response (both amplitude and phase) of the RCMS only changes with applied voltage (i.e., when the spacing d is changed) for x polarization [Fig. 2(g)]. As such, the reflection spectra are presented for x polarization only. The E-field polarization direction is accordance with the arrow direction shown in Fig. 2(g). In order to measure the reflection response of the RCMS, both the rectangular pads are connected to the SMU, and all the cantilever beams are under the same external voltage. However, for the SW measurement, only one pad connected to the SMU, and the other one is not. By doing so, the cantilevers connected to the pad can be deformed under the electrostatic force between the beam and the substrate.

5. RESULTS AND DISCUSSION

As described above, a DC voltage applied to the RCMS actuates the cantilevers. In turn, the deformation of the cantilevers (corresponding to a change in d) modulates the amplitude and phase of the reflected wave. For the initial characterization, we applied a uniform DC voltage to the RCMS using both rectangular pads so that all of the cantilevers are actuated in every column and measured the change in reflectivity from 0 to 52 V. Figures 3(a)–3(c) shows the experimentally measured reflectivity and phase at different DC voltages with the THz pulses at normal incidence (dashed blue lines). The simulation results (red solid lines) use full wave simulations (CST Microwave Studio 2020). In our model, the 20 μm slightly N-doped silicon substrate serves as the spacer layer and is treated as a lossy dielectric material with a permittivity of 11.6 and a loss tangent of 0.07 from 0.5 to 0.75 THz. The 400 nm silicon nitride film served as an insulating layer and was modeled as a lossless dielectric material with permittivity $\varepsilon = 7$. The copper cantilever structure was modeled as a lossy metal with conductivity $\sigma = 5.8 \times 10^7$ S/m. The ground plane and pads were made with gold and modeled as a lossy metal with $\sigma = 4.6 \times 10^7$ S/m. The tip height was adjusted in simulation to match the experimental results for different applied voltages. The simulated amplitude and phase of the reflection response are depicted in Figs. 3(a)–3(c) with solid red lines.

As can be seen from Figs. 3(a)–3(c), the experimental (dashed blue lines) and simulation results (solid red lines) agree well with each other. The slight difference in the reflectivity and phase between the experimental and simulation results arise from fabrication imperfections and measurement errors. At the initial state ($V = 0\,V$), the resonance is at 0.67 THz, and a full-span (2π) phase shift is achieved from 0.5 to 0.75 THz [Fig. 3(a)]. As shown in Figs. 3(b) and 3(c), the resonance frequency of the metasurface redshifts from 0.67 THz ($V = 0\,V$) to 0.64 THz ($V = 45\,V$) and finally to 0.56 THz ($V_{\text{PI}} = 52\,V$). Importantly, at $\sim$0.6 THz, with our RCMS design, we can achieve the full-span phase modulation from the initial state to the pull-in state without any phase discontinuity from the underdamped region ($\Delta Q < 0$) to the overdamped region ($\Delta Q > 0$), meaning gradual phase change and full-span (2π) coverage for all cases. The simulated surface current and electric field distribution [Figs. 3(d) and 3(e)] provides insight into the EM response of the RCMS. For the initial state ($V = 0\,V$), the on-resonance current is mainly on the copper cantilever, corresponding to a LC resonance. The electric field distribution in Fig. 3(e) shows that the electric field is concentrated between the gold pad and the cantilever structure, and the tip-pad structure is the dominant capacitance. The tip-height distance (d) is changed in the simulations to match the experimental results with different applied voltages, indicating that the reflectivity and phase change originate from the increase in the applied voltages and deformation of the cantilever structures. That is, the change in the EM response arises from the voltage-induced change in the tip-pad capacitance.

The excellent agreement between experiments and simulations in Fig. 3 is such that we can further analyze the EM response, where we will consider changes in the reflected amplitude and phase at an operational frequency of 0.6 THz. As we will show, this is a frequency where a large change in the phase and with relatively minor changes in the reflection occur. Figure 4(a) replots the reflection simulations from Fig. 3 in a single panel, while Fig. 4(c) shows a color plot of the reflectivity, which shows that by increasing the applied DC voltage (corresponding to a continuous decrease of the tip height d), the resonance frequency continuously redshifts from 0.67 to 0.56 THz. There is, of course, a corresponding change in the phase as shown in Figs. 4(b) and 4(d). Importantly, the observed changes with voltage are continuous since $\Delta Q < 0$ is maintained (see Section 2 above for discussion). However, due to the pull-in effect of the cantilever structure, the tip height (d) cannot continuously change. This is evident from Fig. 2(i), where the experimental measurement of the cantilever tip height changes quite rapidly for voltages above $\sim$40 V, making precision control difficult (Supplement 1). In particular, between 0 to $\sim$50 V, the cantilever tip displacement decreases from 1.2 μm, which is the initial tip height, to 0.7 μm. At the pull-in voltage ($V_{\text{PI}} = 52\,V$), the cantilevers are pulled down to the gold capacitive pad on the substrate, preventing further deformation of the beam.

Because of the sensitivity of the tip height of d with voltage, the amplitude and phase response in the black shaded region of Figs. 4(c) and 4(d) cannot be utilized with our current RCMS.

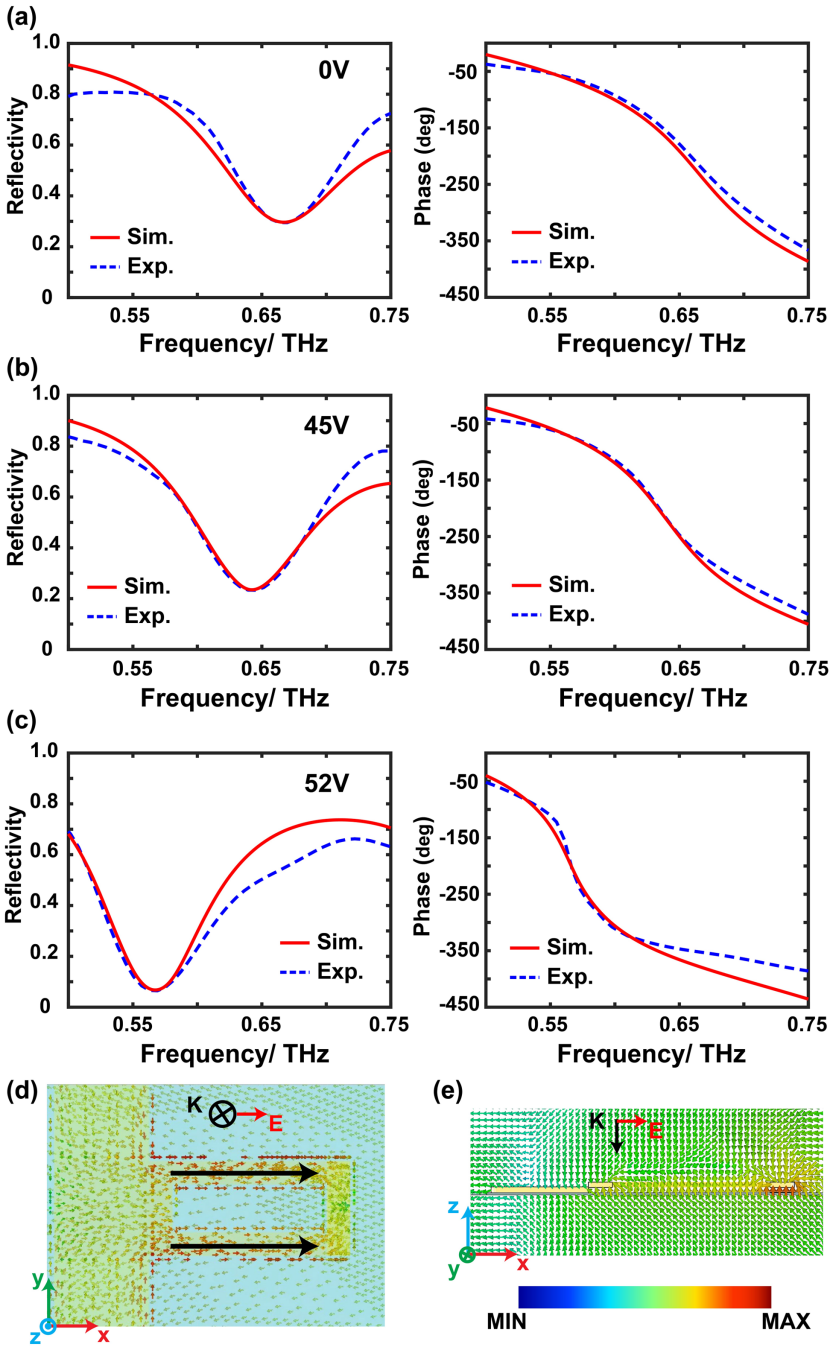

Fig. 3. (a)–(c) Amplitude (left) and phase (right) of the reflectivity for the RCMS at different voltages. (a) $V = 0V$; (b) $V = 45V$; (c) $V = 52V$. The solid red lines are simulations, while the dashed blue lines are experimental results. (d)–(e) On resonance simulated current and electric field distribution, respectively, for the initial state (applied voltage $V = 0V$).

Nonetheless, the RCMS still achieves a full-span (2π) phase modulation over a certain frequency band. As shown in Figs. 4(a) and 4(c) with red, green, and blue stars at 0.6 THz, the amplitude changes in the range of 0.3 to 0.7 between the pull-in state (blue) and the initial state (red). The amplitude change could be further minimized with optimized cantilever structures (i.e., by making ΔQ even smaller). Meanwhile, as shown in Figs. 4(b) and 4(d), the phase changes from -100° ($V_1 = 0V$) to $-120°$ ($V_2 = 45\ V$) and finally to $-306°$ at the pull-in voltage ($V_3 = 52V$). Importantly, most of the phase change occurs between the green and blue stars, where the cantilever changes to the pull-in state. Although the mechanical limits of the cantilever restricts a large tuning range, the RCMS can still act as an on/off switch where phase difference between the initial state (red star) and the pull-in state (blue star) is almost π at 0.6 THz. As we now discuss, this is sufficient to create an on/off surface wave switching for normal incidence THz radiation over a specified frequency band.

The RCMS can realize the switching between a PW and a SW with controlled external voltage on each line. As we discussed above in Section 3, only the cantilevers connected with the top pad will be pulled in, while the other cantilevers remain at the initial position (see Supplement 1 and Visualization 1 for detailed SW generation

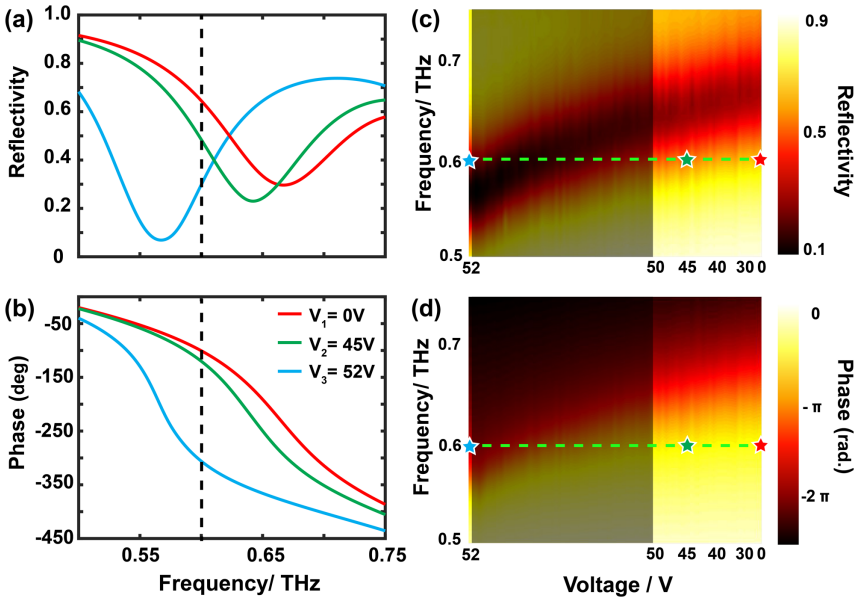

Fig. 4. Amplitude and phase changes of the RCMS with voltage (a) The reflectivity at three different voltages ($V_1 = 0$ V, $V_2 = 45$ V, and $V_3 = 52$ V). (b) The corresponding phase spectrum at the three different voltages. The dashed black line is at 0.6 THz in (a) and (b). (c) and (d) The continuously modulated reflectivity and phase response of the RCMS at different voltages. The shaded region shows the inaccessible portion of the RCMS EM response due to the intrinsic properties of the cantilever structure. The dashed green line shows the 0.6 THz response in accordance with dashed black line (a) and (b), with the red, green, and blue stars corresponding to three different voltages, V_1, V_2, and V_3, respectively.

with RCMS). By doing so, a π phase difference between the adjacent lines is achieved.

The metasurface response under "ON" and "OFF" states are measured with the THz-TDS system, and the results are shown in Fig. 5(a) as dashed blue lines. Clearly, compared with the "OFF" state, the reflectivity is decreased when the metasurface is in the "ON" state since, for a range of frequencies, the light is directed along the surface and not toward the detector. The working

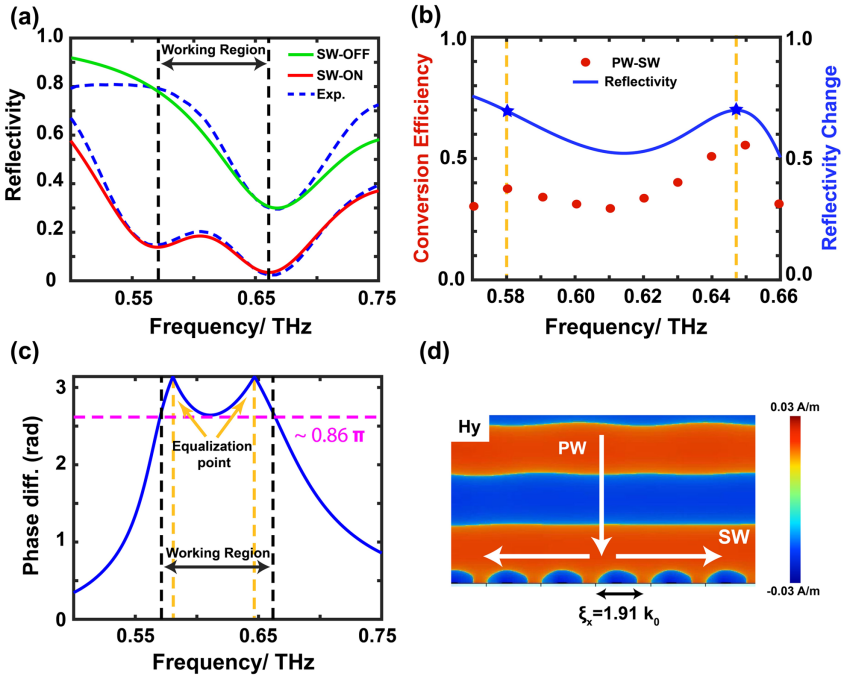

Fig. 5. Generating a SW with a normal incidence PW with the RCMS device. (a) Reflection spectrum when switching between SW and PW. The dashed blue lines show the experimental results from THz-TDs. The red line and the green line are simulations of the "ON" and "OFF" states, respectively. The dashed black line shows the working region, where over 50% of the incident energy is converted to a SW. (b) Conversion efficiency from PW to SW (red dots) and overall reflectivity change (blue line). The red dots show the conversion efficiency as a function of frequency from 0.57 to 0.66 THz. The blue star shows the equalization points where the maximum reflectivity change occurred. (c) The phase difference between two adjacent unit cells when the metasurface is in the "ON" state. The dashed orange line shows the equalization points where the phase difference equals to π. (d) H_y field distributions with phase information on the $\xi_x = 1.91k_0$ (0.65 THz) MEMS-based metasurface.

bandwidth is shown in Fig. 5(a) between the two dashed vertical black lines (0.57 THz to 0.66 THz). The working bandwidth (PW to SW) is determined by the conversion efficiency between the PW and SW [Fig. 5(b) red dots], the phase difference between the adjacent cantilevers [Fig. 5(c)], and finally confirmed with finite element simulation results showing the H_y component of the field [Fig. 5(d)]. As shown in Fig. 5(b), the reflectivity change is first calculated using the reflectivity spectrum measured in Fig. 5(a). The reflectivity change is defined as $(R_{\text{off}} - R_{\text{on}})/R_{\text{off}}$, where R_{off} (green line) and R_{on} (red line) are the reflectivity of the "OFF" and "ON" states, respectively. The conversion efficiency between the PW to SW is further calculated using CST Microwave Studio with the power flow monitor at ten different frequency points. We illuminate the "ON" state RCMS by a normal incidence PW with total power P_{in} and integrate the SW energy within the air–metasurface region to obtain the total outgoing power P_s carried by the SW. The calculated PW-SW conversion efficiency is defined as P_s/P_{in} and is shown as red dots in Fig. 5(b). The results demonstrate that when the RCMS is on the "ON" state, it can efficiently convert an incident PW to a bounded SW with $\sim 60\%$ at 0.65 THz and greater than 30% over the operational bandwidth (0.57–0.66 THz). Figure 5(c) shows the phase difference between the two adjacent cantilevers as the function of the frequency in the "ON" state. Clearly, the maximum conversion efficiency occurs at the equalization point [dashed orange line and blue stars in Figs. 5(b) and 5(c), respectively], where the phase difference equals to π (180°). Also, when the phase difference is larger than 0.86π ($\sim$150°, dashed pink line), more than 30% of the energy from the PW can be converted into the SW. Figure 5(d) shows the simulated H_y field (including phase information) in the "ON" state metasurface under normal incidence PW at 0.65 THz. From the H_y-field distribution in Fig. 5(d), we can clearly see from the patterns that the H_y field has a well-defined 2π periodicity $\xi_x = 1.91k_0$. The simulated H_y field also exhibits a well-defined parallel k vector at the air–metasurface interface. The simulation results indicate that when the PW illuminates the RCMS in the "ON" state, the "reflected" wave cannot reflect back to the free space and becomes a SW and trapped by the metasurface due to $\xi > k_0$ (see Supplement 1 for a detailed field distribution and the pure scattered field pattern). The simulation results also explain the changes in the reflectivity between the "ON" and "OFF" state in Fig. 5(a).

Further optimization of our MEMS-based metasurface can be pursued to increase the reflection amplitude, tuning range, and realization of finer control at the unit cell level with well-designed signal routing strategies. For example, there have been efforts to increase the reflection amplitude and increase the tuning range with novel cantilever designs and larger tip-height distances [53,61]. Moreover, silicon via (TSV) and other well-designed routing strategies are mature in most CMOS applications [62] and can, in future designs, be used in MEMS-based metasurfaces to realize precision control at the single unit cell level.

6. CONCLUSION

In conclusion, we have successfully demonstrated that surface waves can be generated on demand with our RCMS by realizing full-span (2π) phase modulation and single line control of the cantilever-based unit cell. By realizing the line-by-line control of the metasurface, we can achieve a π phase difference between the adjacent cantilevers and with two-unit cells, covering the entire 2π phase range. The conversion efficiency, from the PW to SW, of our RCMS is nearly 60% at the maximum point and over 30% over an approximately 100 GHz bandwidth. Compared with previous works on MEMS-based metasurfaces, our work has realized line-by-line control (1D control) of the metasurface, which is a crucial step toward realizing future dynamical beamforming and focusing devices. More importantly, this work presents a MEMS-based metasurface that can efficiently switch the normal incidence PW to the SW at the air–metasurface interface. Our results will facilitate the development and applications of THz wave modulation and future MIMO 5G communication systems.

Funding. National Science Foundation Division of Electrical, Communications and Cyber Systems (ECCS-1810252); Army Research Office (MURI W911NF-16-1-0361).

Acknowledgment. We acknowledge the Boston University Photonics Center for technical support.

Disclosures. The authors declare no conflicts of interest.

Data Availability. Data underlying the results presented in this paper are not publicly available at this time but may be obtained from the authors upon reasonable request.

Supplemental document. See Supplement 1 for supporting content.

[†]These authors contributed equally to this paper.

REFERENCES

1. A. Ourir, S. N. Burokur, and A. de Lustrac, "Phase-varying metamaterial for compact steerable directive antennas," Electron. Lett. **43**, 493–494 (2007).
2. J. R. Reis, M. Vala, and R. D. S. Caldeirnha, "Review paper on transmitarray antennas," IEEE Access **7**, 94171–94188 (2019).
3. S. Sun, Q. He, S. Xiao, Q. Xu, X. Lin, and L. Zhou, "Gradient-index metasurface as a bridge linking propagating waves and surface waves," Nat. Mater. **11**, 426–431 (2012).
4. H. T. Chen, A. J. Taylor, and N. Yu, "A review of metasurface: physics and applications," Rep. Prog. Phys. **79**, 076401 (2016).
5. N. Yu and F. Capasso, "Flat optics with designer metasurfaces," Nat. Mater. **13**, 139–150 (2014).
6. A. Epstein and G. V. Eleftheriades, "Huygens' metasurfaces via the equivalence principle: design and applications," J. Opt. Soc. Am. B **33**, A31–A50 (2016).
7. J. A. Perreault, T. G. Bifano, B. M. Levine, and M. N. Horenstein, "Adaptive optic correction using micro-electro-mechanical deformable mirrors," Opt. Eng. **41**, 561–566 (2002).
8. T. J. Yen, W. J. Padilla, N. Fang, D. C. Vier, D. R. Smith, J. B. Pendry, D. N. Basov, and X. Zhang, "Terahertz magnetic response from artificial materials," Science **303**, 1494–1496 (2004).
9. J. Valentine, S. Zhang, T. Zentgraf, E. Ulin-Avila, D. A. Genov, G. Bartal, and X. Zhang, "Three-dimensional optical metamaterial with a negative refractive index," Nature **455**, 376–379 (2008).
10. S. Zhang, Y. S. Park, J. Li, X. Lu, W. Zhang, and X. Zhang, "Negative refractive index in chiral metamaterials," Phys. Rev. Lett. **102**, 023901 (2009).
11. K. Fan, I. V. Shadrivov, A. E. Miroshnichenko, and W. J. Padilla, "Infrared all-dielectric Kerker metasurface," Opt. Express **29**, 10518–10526 (2021).
12. J. B. Pendry, "Negative refraction makes a perfect lens," Phys. Rev. Lett. **85**, 3966–3969 (2000).
13. R. A. Shelby, D. R. Smith, and S. Schultz, "Experimental verification of a negative index of refraction," Science **292**, 77–79 (2001).
14. D. R. Smith, S. Schultz, P. Markoš, and C. M. Soukoulis, "Determination of effective permittivity and permeability of metamaterials from reflection and transmission coefficients," Phys. Rev. B **65**, 195104 (2002).
15. T. Koschny, P. Markoš, D. R. Smith, and C. M. Soukoulis, "Resonant and antiresonant frequency dependence of the effective parameter of metamaterials," Phys. Rev. E **68**, 065602 (2003).

16. A. Alù, A. Salandrino, and N. Engheta, "Negative effective permeability and left-handed materials at optical frequencies," Opt. Express **14**, 1557–1567 (2006).
17. C. Chen, Y. Huang, K. Wu, T. G. Bifano, S. W. Anderson, X. Zhao, and X. Zhang, "Polarization insensitive, metamaterial absorber-enhanced long-wave infrared detector," Opt. Express **28**, 28843–28857 (2020).
18. M. Wu, X. Zhao, J. Zhang, J. Schalch, G. Duan, K. Cremin, R. D. Averitt, and X. Zhang, "A three-dimensional all-metal terahertz metamaterial perfect absorber," Appl. Phys. Lett. **111**, 051101 (2017).
19. I. J. Luxmoore, P. Q. Liu, P. Li, J. Faist, and G. R. Nash, "Graphene-metamaterial photodetectors for integrated infrared sensing," ACS Photon. **3**, 936–941 (2016).
20. D. Neshev and I. Aharonovich, "Optical metasurfaces: new generation building blocks for multifunctional optics," Light Sci. Appl. **7**, 58 (2018).
21. H. H. Hsiao, C. H. Chu, and D. P. Tsai, "Fundamentals and applications of metasurfaces," Small Methods **1**, 1600064 (2017).
22. M. Khorasaninejad, F. Aieta, P. Kanhaiya, M. A. Kats, P. Genevet, D. Rousso, and F. Capasso, "Achromatic metasurface lens at telecommunication wavelengths," Nano Lett. **15**, 5358–5362 (2015).
23. N. Yu, P. Genevet, M. A. Kats, F. Aieta, J. P. Tetienne, F. Capassso, and Z. Gaburro, "Light propagation with phase discontinuities: generalized laws of reflection an refraction," Science **334**, 333–337 (2011).
24. X. Guo, Y. Ding, X. Chen, Y. Duan, and X. Ni, "Molding free-space light with guided wave-driven metasurfaces," Sci. Adv. **6**, eabb4142 (2020).
25. X. Guo, Y. Ding, Y. Duan, and X. Ni, "Nonreciprocal metasurface with space-time phase modulation," Light Sci. Appl. **8**, 123 (2019).
26. A. K. Azad, A. V. Efimov, S. Ghosh, J. Singleton, A. J. Taylor, and H. T. Chen, "Ultra-thin metasurface microwave flat lens for broadband applications," Appl. Phys. Lett. **110**, 224101 (2017).
27. A. V. Kildishev, A. Boltasseva, and V. M. Shalaev, "Planar photonics with metasurfaces," Science **339**, 1232009 (2013).
28. S. Walia, C. M. Shah, P. Gutruf, H. Nili, D. R. Chowdhury, W. Withayachumnankul, M. Bhaskaran, and S. Sriram, "Flexible metasurfaces and metamaterials: a review of materials and fabrication processes at micro- and nano scales," Appl. Phys. Rev. **2**, 011303 (2015).
29. S. Sun, K. Y. Yang, C. M. Wang, T. K. Juan, W. T. Chen, C. Y. Liao, Q. He, S. Xiao, W. T. Kung, G. Y. Guo, L. Zhou, and D. P. Tsai, "High-efficiency broadband anomalous reflection by gradient metasurfaces," Nano Lett. **12**, 6223–6229 (2012).
30. C. Pfeiffer, N. K. Emani, A. M. Shaltout, A. Boltasseva, V. M. Shalaev, and A. Grbic, "Efficient light bending with isotropic metamaterial Huygens' surfaces," Nano Lett. **14**, 2491–2497 (2014).
31. F. Aieta, P. Genevet, M. A. Kats, N. Yu, R. Blanchard, Z. Gaburro, and F. Capasso, "Aberration-free ultrathin flat lenses and axicons at telecom wavelengths based on plasmonic metasurfaces," Nano Lett. **12**, 4932–4936 (2012).
32. N. M. Estakhri and A. Alù, "Recent progress in gradient metasurfaces," J. Opt. Soc. Am. B **33**, A21–A30 (2016).
33. W. Luo, S. Xiao, Q. He, S. Sun, and L. Zhou, "Photonic spin hall effect with nearly 100% efficiency," Adv. Opt. Mater. **3**, 1102–1108 (2015).
34. W. Dong, Y. Qiu, X. Zhou, A. Banas, K. Banas, M. B. H. Breese, T. Cao, and R. E. Simpson, "Tunable mid-infrared phase-change metasurface," Adv. Opt. Mater. **6**, 1701346 (2018).
35. M. Liu, H. Y. Hwang, H. Tao, A. C. Strikwerda, K. Fan, G. R. Keiser, A. J. Sternbach, K. G. West, S. Kittiwatanakul, J. Lu, S. A. Wolf, F. G. Omenetto, X. Zhang, K. A. Nelson, and R. D. Averitt, "Terahertz-field-induced insulator-to-metal transition in vanadium dioxide metamaterial," Nature **487**, 345–348 (2012).
36. V. S. A. Varri, D. Tripathi, H. S. Vyas, P. Agarwal, and R. S. Hegde, "Optically-reconfigurable phase change material nanoantenna-embedded metamaterial waveguide," Opt. Mater. Express **11**, 988–1003 (2021).
37. X. Zhao, Y. Wang, J. Schalch, G. Duan, K. Cremin, J. Zhang, C. Chen, R. D. Averitt, and X. Zhang, "Optically modulated ultra-broadband all-silicon metamaterial terahertz absorbers," ACS Photon. **6**, 830–837 (2019).
38. Z. Miao, Q. Wu, X. Li, Q. He, K. Ding, Z. An, Y. Zhang, and L. Zhou, "Widely tunable terahertz phase modulation with gate-controlled graphene metasurfaces," Phys. Rev. X **5**, 041027 (2015).
39. X. He and S. Kim, "Tunable terahertz graphene metamaterials," Carbon **82**, 229–237 (2015).
40. X. Zhao, J. Zhang, K. Fan, G. Duan, J. Schalch, G. R. Keiser, R. D. Averitt, and X. Zhang, "Electromechanically tunable metasurface transmission waveplate at terahertz frequencies," Optica **5**, 303–310 (2018).
41. X. Zhao, J. Zhang, K. Fan, G. Duan, J. Schalch, G. R. Keiser, R. D. Averitt, and X. Zhang, "Real-time tunable phase response and group delay in broadside coupled split-ring resonators," Phys. Rev. B **99**, 245111 (2019).
42. L. Cong, P. Pitchappa, Y. Wu, L. Ke, C. K. Lee, N. Singh, H. Yang, and R. Singh, "Active multifunctional microelectromechanical system metadevices: applications in polarization control, wavefront deflection, and holograms," Adv. Opt. Mater. **5**, 1600716 (2016).
43. H. Tao, A. C. Strikwerda, K. Fan, W. J. Padilla, X. Zhang, and R. D. Averitt, "Reconfigurable terahertz metamaterials," Phys. Rev. Lett. **103**, 147401 (2009).
44. X. Zhao, K. Fan, J. Zhang, G. R. Keiser, G. Duan, R. D. Averitt, and X. Zhang, "Voltage-tunable dual-layer terahertz metamaterials," Microsyst. Nanoeng. **2**, 1–8 (2016).
45. W. M. Zhu, A. Q. Liu, X. M. Zhang, D. P. Tsai, T. Bourouina, J. H. Teng, X. H. Zhang, H. C. Guo, H. Tanoto, T. Mei, G. Q. Lo, and D. L. Kwong, "A flat lens with tunable phase gradient by using random access reconfigurable metamaterial," Adv. Mater. **27**, 4739–4743 (2015).
46. N. I. Zheludev and Y. S. Kivshar, "From metamaterials to metadevices," Nat. Mater. **11**, 917–924 (2012).
47. X. Zhao, G. Duan, A. Li, C. Chen, and X. Zhang, "Integrating microsystems with metamaterials towards metadevices," Microsyst. Nanoeng. **5**, 1–17 (2019).
48. Y. Liu and X. Zhang, "Metamaterials: a new frontier of science and technology," Chem. Soc. Rev. **40**, 2494–2507 (2011).
49. T. Kan, A. Isozaki, N. Kanda, N. Nemoto, K. Konishi, M. Kuwata-Gonokami, K. Matsumoto, and I. Shimoyama, "Spiral metamaterial for active tuning of optical activity," Appl. Phys. Rev. **102**, 221906 (2013).
50. P. C. Wu, W. Zhu, Z. Shen, P. H. J. Chong, W. Ser, D. P. Tsai, and A. Q. Liu, "Broadband wide-angle multifunctional polarization converter via liquid-metal-based metasurface," Adv. Opt. Mater. **5**, 1600938 (2017).
51. E. Arbabi, A. Arbabi, S. M. Kamali, Y. Horie, M. Faraji-Dana, and A. Faraon, "MEMS-tunable dielectric metasurface lens," Nat. Commun. **9**, 812 (2018).
52. H. S. Ee and R. Agarwal, "Tunable metasurface and flat optical zoom lens on a stretchable substrate," Nano Lett. **16**, 2818–2823 (2016).
53. T. Kan, A. Isozaki, N. Kanda, N. Nemoto, K. Konishi, H. Takahashi, M. Kuwata-Gonokami, K. Matsumoto, and I. Shimoyama, "Enantiomeric switching of chiral metamaterial for terahertz polarization modulation employing vertically deformable MEMS spirals," Nat. Commun. **6**, 8422 (2015).
54. Y. Shen, X. Wang, Z. Xie, C. Min, X. Fu, Q. Liu, M. Gong, and X. Yuan, "Optical vortices 30 years on: OAM manipulation from topological charge to multiple singularities," Light Sci. Appl. **8**, 90 (2019).
55. C. Qu, S. Ma, J. Hao, M. Qiu, X. Li, S. Xiao, Z. Miao, N. Dai, Q. He, S. Sun, and L. Zhou, "Tailor the functionalities of metasurface based on a complete phase diagram," Phys. Rev. Lett. **115**, 235503 (2015).
56. R. Xu, X. Xu, B. R. Yang, X. Gui, Z. Qin, and Y. S. Lin, "Actively logical modulation of MEMS-based terahertz metamaterial," Photon. Res. **9**, 1409–1415 (2021).
57. J. Zhong, X. Xu, and Y. S. Lin, "Tunable terahertz metamaterial with electromagnetically induced transparency characteristic for sensing application," Nanomaterials **11**, 2175 (2021).
58. Z. Ren, Y. Chang, Y. Ma, K. Shih, B. Dong, and C. Lee, "Leveraging of MEMS technologies for optical metamaterials applications," Adv. Opt. Mat. **8**, 1900653 (2019).
59. G. Duan, J. Schalch, X. Zhao, A. Li, C. Chen, R. D. Averitt, and X. Zhang, "A survey of theoretical models for terahertz electromagnetic metamaterial absorbers," Sens. Actuators A **287**, 21–28 (2019).
60. W. L. Barnes, A. Dereux, and T. W. Ebbesen, "Surface plasmon subwavelength optics," Nature **424**, 824–830 (2003).
61. Z. Han, K. Kohno, H. Fujita, K. Hirakawa, and H. Toshiyoshi, "MEMS reconfigurable metamaterial for terahertz switchable filter and modulator," Opt. Express **22**, 21326–21339 (2014).
62. E. Beyne, P. De Moor, W. Ruythooren, R. Labie, A. Jourdain, H. Tilmans, D. S. Tezcan, P. Soussan, B. Swinnen, and R. Cartuyvels, "Through-silicon via and die stacking technologies for microsystems-integration," in *IEEE International Electron Devices Meeting* (2008), pp. 495–498.